Nanoscale

COMMUNICATION

Check for updates

Well-defined Co_9S_8 cages enable the separation of photoexcited charges to promote visible-light CO_2 reduction†

Xiahui Lin, Zidong Xie, Bo Su, Mei Zheng, Wenxin Dai, [iD] Yidong Hou, [iD] Zhengxin Ding,* Wei Lin, [iD] * Yuanxing Fang [iD] * and Sibo Wang [iD] *

Exploring affordable cocatalysts with high performance for boosting charge separation and CO_2 activation is an effective strategy to reinforce CO_2 photoreduction efficiency. Herein, well-defined Co_9S_8 cages are exploited as a nonprecious promoter for visible-light CO_2 reduction. The Co_9S_8 cages are prepared *via* a multistep strategy with ZIF-67 particles as the precursor and fully characterized by physicochemical techniques. The hollow Co_9S_8 cocatalyst with a high surface area and profuse catalytically active centers is discovered to accelerate separation and transfer of light-induced charges, and strengthen concentration and activation of CO_2 molecules. In a hybrid photosensitized system, these Co_9S_8 cages efficiently promote the deoxygenative reduction of CO_2 to generate CO, with a high yield rate of 35 μmol h^{-1} (*i.e.*, 35 mmol h^{-1} g^{-1}). Besides, this cocatalyst is also of high stability for the CO_2 photoreduction reaction. Density functional theory (DFT) calculations reveal that the Ru(bpy)$_3^{2+}$ photosensitizer is strongly absorbed on the Co_9S_8 (311) surface through forming four Co–C bonds, which can serve as the "bridges" to ensure quick electron transfer from the excited photosensitiser to the active Co_9S_8 cocatalyst, thus promoting the separation of photoexcited charges for ehannced CO_2 reduction performance.

*State Key Laboratory of Photocatalysis on Energy and Environment, College of Chemistry, Fuzhou University, FujianFuzhou, 350002, China.
E-mail: zxding@fzu.edu.cn, wlin@fzu.edu.cn, yxfang@fzu.edu.cn, sibowang@fzu.edu.cn*

Yuanxing Fang went to the University of Sussex, United Kingdom, to study chemistry, and obtained his MChem degree in 2012 and PhD degree in 2017. He went to the State Key Laboratory of Photocatalysis on Energy and Environment at Fuzhou University, P. R. China, as a Postdoctoral fellow in 2017. In 2019, he was appointed as Associated Professor in the College of Chemistry, Fuzhou University, and promoted to

Yuanxing Fang

Special Professor in 2021. His longstanding interests are the developments of photocatalytic and photoelectrochemical devices for energy and environmental applications, such as water splitting, CO_2 reduction, organosynthesis and others. He has published more than 45 peer-reviewed publications, which have garnered more than 2000 citations and an H-index of 21.

Solar-driven CO_2 reduction, an ideal strategy to afford low-carbon fuels (*i.e.*, CO and CH_4) with renewable energy, is long being intensively studied,[1–6] given its promise in addressing the issues of energy and environment. However, as limited by the extreme chemical inertness of linear CO_2 molecules, the easy recombination feature of photoexcited charges and the intricacy of the multi-electron/proton engaged reaction,[7–10] photocatalytic CO_2 reduction currently suffers from low efficiency coupled with moderate selectivity that is far behind the criteria of practical utilization.

During the past few decades, a great deal of strategies have been proposed to improve CO_2 photoreduction efficiency with inspiring progress realized.[11–16] Therein, cocatalyst engineering is verified to be a preferred approach. This is because cocatalysts can enable capture and activation of CO_2 molecules, accelerate separation and transfer kinetics of charge carriers, and provide catalytically active sites to selectively operate the redox reactions.[17,18] The noble metal nanoparticles are the classic CO_2 reduction cocatalysts with high catalytic performance,[19–22] and alternatively, the transition metal ions/complexes of cobalt and nickel can serve as efficient promoters for CO_2 photoreduction in cooperation with specific light-sensitizers.[23–30] Comparatively, considering the requirements of large-scale execution (*i.e.*, low price, high abundance, easy

separation/retrieval), exploring heterogeneous cocatalysts composed of cost-affordable elements for CO_2 photoreduction is highly desirable.

Besides the chemical composition, designing catalytic materials with favored architectures is also of vital importance for photocatalytic CO_2 reduction.[31] As a group of multifunctional catalysts for energy storage and conversion,[32,33] hollow structures are actively employed for CO_2 photoreduction,[34–40] owing to their inherent advantages, such as a shortened perpendicular path for charge transfer to prevent their recombination, plentiful surface-active sites to boost CO_2 capture and redox catalysis, and strengthened interior reflection/scattering to enhance incident light utilization.[41–43]

With all the aforementioned concerns in mind, in this work, the well-defined Co_9S_8 cages are applied as a cocatalyst coupled with $Ru(bpy)_3^{2+}$ (abbreviated as Ru, bpy = 2'2-bipyridine) as a photosensitizer for CO_2 reduction under visible light. The dodecahedral Co_9S_8 cage is created *via* a multi-step method as depicted schematically in Fig. 1. Starting with Co_2^+ and 2-methylimidazole as the raw materials, the zeolitic imidazolate framework (ZIF)-67 dodecahedron is first prepared through a reported precipitation method with some adjustments (step I).[44,45] Next, the ZIF-67 particle is converted to a CoS_x cage by a hydrothermal sulfidation reaction (step II). Finally, the Co_9S_8 cage is harvested after annealing the CoS_x intermediate under a N_2 atmosphere at 550 °C (step III).

The Co_9S_8 cocatalyst is revealed by diverse photo-/electrochemical tests to augment CO_2 activation and promote separation of light-excited charges. In a tandem photochemical system, the Co_9S_8 cocatalyst enables the deoxygenative reduction of CO_2 by visible light, with a CO formation rate of 35 $\mu mol\ h^{-1}$, under the cooperation of $Ru(bpy)_3^{2+}$ as a photosensitizer. Indeed, the reduction ability of the Co_9S_8 catalyst in photocatalysis has been demonstrated by hydrogen evolution reactions;[46–50] however, its talent for CO_2 photoreduction has been seldom exploited so far.

Production of the ZIF-67 precursor was confirmed by powder X-ray diffraction (XRD) and energy-dispersive X-ray (EDX) characterization (Fig. S1, ESI†). The field emission scanning electron microscopy (FESEM) images show that the as-synthesized ZIF-67 particles present a morphology of nearly monodisperse dodecahedra with high uniformity (Fig. 2a and b).

After the sulfidation treatment, the ZIF-67 precursor was entirely transformed into an amorphous cobalt sulfide (CoS_x) product with a Co/S ratio of about 1 : 3.42 (Fig. S2, ESI†). The
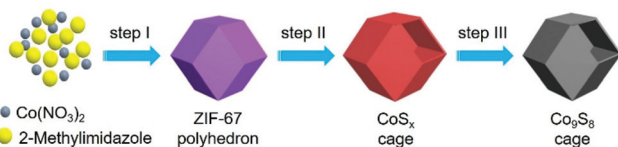

Fig. 2 (a and b) FESEM images of ZIF-67 dodecahedra. (c–e) FESEM images and (f) TEM image of CoS_x cages.

FESEM images indicate that the CoS_x intermediate can inherit the dodecahedral shape of the parental ZIF-67 particles perfectly (Fig. 2c). From the magnified FESEM images (Fig. 2d and e), it is found that the CoS_x particles have a relatively rougher surface than the ZIF-67 precursor, and the observed clear cavity of the broken CoS_x dodecahedra implies their hollow structure. The empty interior of the well-defined CoS_x cages is then confirmed visually by the TEM image (Fig. 2f). The possible formation process of CoS_x cages is clarified as follows. During the hydrothermal sulfidation reaction, the thioacetamide is decomposed to release the sulfide ions to react with the cobalt ions on the ZIF-67 particle surface, yielding an outermost layer of CoS_x. Further formation of the CoS_x shell continues *via* the reactions between inward diffusing sulfide ions and outward diffusing metal ions, finally producing the polyhedral CoS_x cages.[46,51]

The CoS_x material was treated by annealing in N_2 to attain the Co_9S_8 product. To monitor the conversion procedure, thermogravimetry (TG) analysis was conducted. As shown in

Fig. 1 Schematic illustration of the preparation processes of dodecahedral Co_9S_8 cages: (I) self-assembly, (II) sulfidation, and (III) annealing in N_2.
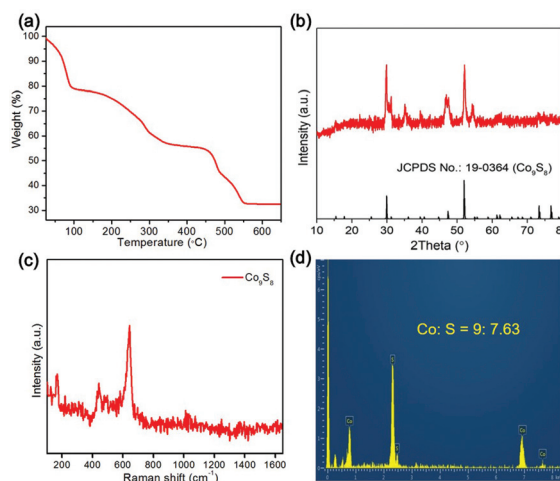

Fig. 3 (a) TG curve of CoS_x cages in in N_2. (b) XRD pattern, (c) Raman spectrum and (d) EDX spectrum of Co_9S_8 cages.

Fig. 3a, the result of TG indicates that the CoS_x intermediate undergoes gradual weight loss during the thermal treatment due to sulphur volatilization, and finally forms a stable product at 550 °C, which is confirmed to be the Co_9S_8 phase (JCPDS card no.: 19-0364) by XRD analysis (Fig. 3b). No impurity XRD peaks are discerned, signifying the high phase purity of the Co_9S_8 material. The Raman spectrum of the Co_9S_8 sample presents a distinct vibrational peak at around 640 cm^{-1} together with a set of bands below 750 cm^{-1} (Fig. 3c), indexing to the characteristic Raman peaks of the Co_9S_8 phase.[52,53] The EDX spectrum shows that the Co_9S_8 product is only composed of Co and S elements with a molar ratio of about 9 : 7.63 (Fig. 3d), which is close to the theoretical value.

The morphology and microstructures of the Co_9S_8 product were researched by FESEM and TEM. As can be seen from the FESEM images (Fig. 4a and b), the Co_9S_8 particles well preserve the pristine polyhedral construction of the CoS_x intermediate without perceptible agglomeration or fractures. The careful FESEM analysis discloses that the surface of Co_9S_8 particles experiences slight shrinkage after the thermal treatment (Fig. 4c). The structural features of Co_9S_8 cages revealed by TEM are consistent with the results of FESEM (Fig. 4d and e). The crystal features of Co_9S_8 cages were then checked by high-resolution TEM (HRTEM) analysis. As shown in Fig. 4f, the HRTEM image displays strong lattice fringes with an interlayer d-spacing of 0.28 nm determined by the corresponding inverse fast Fourier transformation (IFFT) image and line scans (Fig. 4g and h), which is assigned to the (222) crystal plane of the cubic Co_9S_8 phase. The Co_9S_8 product is verified to be a polycrystalline material, as revealed by the selected area elec-

tron diffraction (SAED) pattern (Fig. 4i), in which the clear diffraction fringes are attributed to the interplanar spacings of the cubic Co_9S_8 phase.

The surface chemical states of elements of the Co_9S_8 material were studied by X-ray photoelectron spectroscopy (XPS). As shown in Fig. 5a, the high-resolution Co 2p spectrum is fitted into two sets of spin–orbit doublets and satellite (Sat.) peaks. The first doublet located at 778.3 and 779.4 eV and the second doublet with binding energies of 793.4 and 795.5 eV are attributed to Co $2p_{3/2}$ and Co $2p_{1/2}$, respectively. The presence of these doublets indicates the coexistence of Co^{3+} and Co_2^+, which is in agreement with the results of previous work.[54–56] In the XPS spectrum of S 2p (Fig. 5b), the fitted peaks with binding energies of about 162.1 and 163.1 eV are assigned to the Co–S species, while the other two peaks centered at 163.7 and 164.9 eV are attributable to the S–O bonds,[46] implying the surface oxidation of the Co_9S_8 sample that is generally detected during XPS measurements.

The textural properties of Co_9S_8 cages were examined by N_2 sorption measurements. As displayed in Fig. 5c, classified type-II N_2 adsorption–desorption isotherms together with a type H3 hysteresis loop are observed, suggesting the formation of mesopores in the material, which can be further confirmed by the corresponding pore size distribution plot (inset, Fig. 5c). Generation of the porous structure of Co_9S_8 cages is positive to facilitate mass transportation for heterogeneous photocatalytic applications. The Co_9S_8 material is measured to have a high specific Brunauer–Emmett–Teller (BET) surface area of about 137 $m^2 g^{-1}$, which should be mainly contributed by the well-defined hollow configuration. Such a high surface area will enable the capture and concentration of CO_2 molecules, as reflected by the CO_2 adsorption isotherm, which gives a maximum CO_2 uptake of about 13.5 $cm^3 g^{-1}$ at 0 °C and 1 atm (Fig. 5d). These textural features of Co_9S_8 cages are ben-
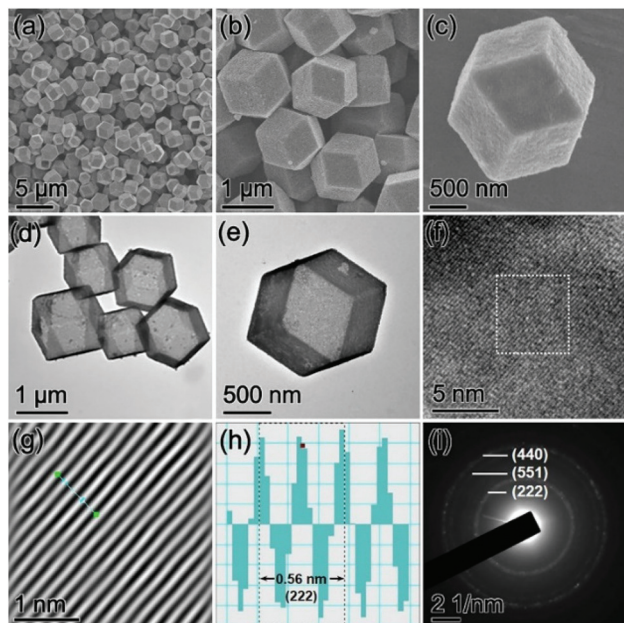

Fig. 4   (a–c) FESEM images, (d and e) TEM images, (f) HRTEM image, (g and h) the corresponding inverse fast Fourier transformation (IFFT) image and line scans of the dotted square region in (f), and (i) SAED pattern of Co_9S_8 cages.
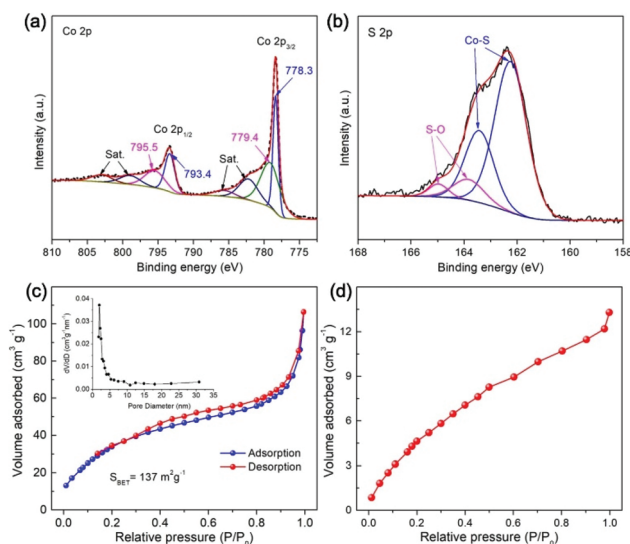

Fig. 5   (a) Co 2p and (b) S 2p XPS spectrum, (c) N_2 adsorption–desorption isotherms, and (d) CO_2 adsorption isotherm of Co_9S_8 cages.

eficial to afford rich exposed catalytically active sites and boost mass transport for heterogeneous CO_2 fixation reactions.

We then evaluated the performance of Co_9S_8 cages by the visible-light CO_2 reduction reaction conducted in a classic hybrid system,[2,25,54,57–61] engaging $Ru(bpy)_3^{2+}$ as the light-harvester and H_2O/acetonitrile/TEOA mixture as the reaction medium. Fig. 6a presents the CO_2 reduction activity of the Co_9S_8 cocatalyst as a function of reaction time. As can be seen, the system manifests a high photocatalytic performance in the initial first 1 h of the reaction, showing a CO_2-to-CO conversion rate of 35 μmol h^{-1}, coupled with a H_2-releasing rate of 12 μmol h^{-1}. In addition to CO and H_2, no detectable formation of hydrocarbon products is observed in the liquid phase. On further continuing the reaction, generation of the products increases progressively, but with a decreased rate, which should result from degradation of the ruthenium photosensitizer.[57,62,63] The total yield of CO reaches 65 μmol after photoreaction for 7 h, corresponding to a catalytic turnover number (TON) of about 54 relative to the cocatalyst.

The working mechanism of the CO_2 reduction system was inspected by controlling the reaction conditions. As shown in Fig. 6b, compared to that of the normal reaction (column 1), the evolution of CO/H_2 reduces significantly once the Co_9S_8 cocatalyst is omitted from the system, highlighting its critical role in promoting the CO_2 reduction reaction. No product is detected without the introduction of a photosensitizer (column 3) or visible light irradiation (column 4), which indicates that the CO_2 reduction reaction is a visible-light-sensitized process. It is revealed that TEOA is essential to achieve the CO_2 reduction photocatalysis, as the reaction would be completely terminated without its participation (column 5), which matches well with the results of reported studies in analogous photochemical systems.[2,25,57,62,64] When employing N_2 as the gas feedstock to substitute CO_2 for running the reaction (column 6), the only product generated is H_2, suggesting that the CO product should be derived from the CO_2 gas.

To directly track the origin of CO, we performed a ^{13}C-labelled reaction with $^{13}CO_2$ as the reactant and analyzed the produced CO by mass spectroscopy (MS). As indicated in Fig. 6c, the MS spectrum manifests a predominant peak with a m/z value of 29, which is attributed distinctly to ^{13}CO. This observation firmly validates the source of CO generation, that is, the CO_2 feedstock.

The CO_2 photoreduction reactions were also initiated with light irradiation of different wavelengths through applying specific long-pass cut-off filters. As revealed in Fig. 6d, the formation of CO/H_2 diminishes gradually under light irradiation of longer wavelengths, because of the decline in the incident photons when extending the wavelength of the light filter. These findings indicate that the CO_2 reduction is motivated by light excitation of the photosensitizer.

To examine the stability of the Co_9S_8 cocatalyst, after CO_2 photoreduction reactions, it was separated, washed, and re-added into fresh reaction mixtures for repeated operations. No apparent decrease in CO/H_2 production is detected during the stability tests (Fig. 6e), pointing to its high activity stability. The results of XRD, FTIR, Raman, and XPS tests for the Co_9S_8 cocatalyst before and after photoreaction expose its high stabilities in the crystal, chemical and surface structures in the photocatalytic CO_2 reduction system (Fig. 6f, and Fig. S3, ESI†).

In order to gain an understanding of the high performance of the CO_2 photoreduction system mediated by Co_9S_8 cages, we carried out photo-/electro-chemical measurements. To demonstrate the function of Co_9S_8 in the CO_2 reduction reaction, linear sweep voltammetry (LSV) was conducted. As shown in Fig. 7a, the Co_9S_8 catalyst delivers a more positive onset potential and a higher cathodic current in CO_2-saturated solution than those under N_2-saturated conditions. These outcomes verify that the Co_9S_8 cages can activate CO_2 molecules and drive their reduction reaction.[63,65]

UV–vis diffuse reflectance spectra (DRS) indicate that the Co_9S_8 cocatalyst and $Ru(bpy)_3^{2+}$ photosensitizer show strong visible light absorption (Fig. 7b), while their hybrid possesses an optical harvesting ability. By using UV-vis DRS and the Tauc curve of Co_9S_8 (Fig. S4, ESI†), its bandgap energy is measured to be 0.98 eV.[37,47] To define the conduction band bottom (CBM) and valence band maximum (VBM) positions, the flat
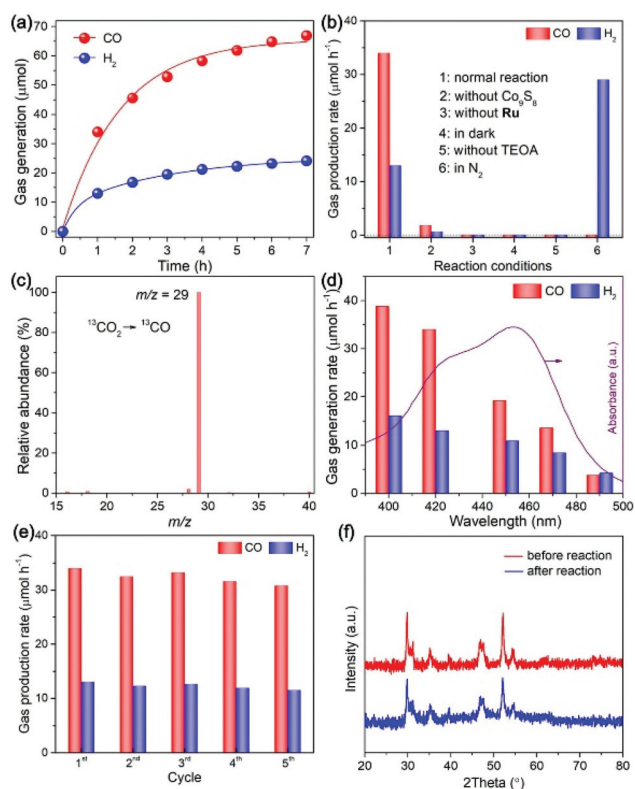

Fig. 6 (a) CO_2 photoreduction activity of the Co_9S_8 cocatalyst as a function of reaction time. (b) Performance of the CO_2 reduction system under various conditions. (c) Mass spectrum of CO yielded from the $^{13}CO_2$ isotope reaction. (d) CO and H_2 generation by visible light with different wavelengths. (e) Stability tests of the Co_9S_8 cocatalyst. (f) XRD patterns of the Co_9S_8 cocatalyst before and after CO_2 reduction reactions.
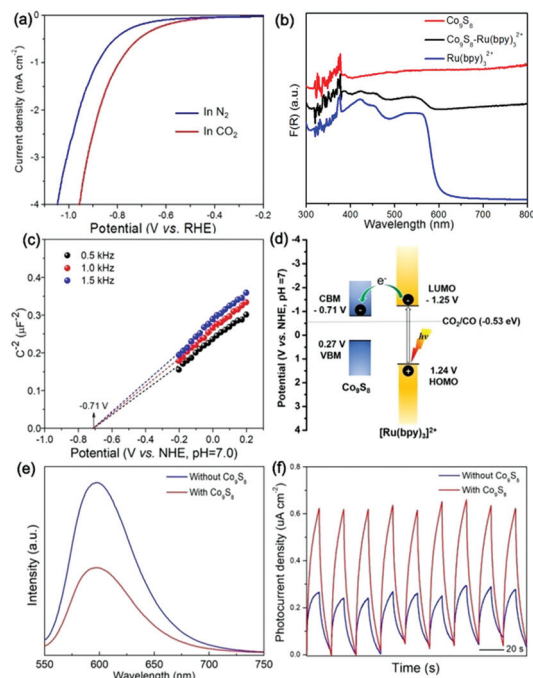
Fig. 7 (a) LSV curve of the Co_9S_8 cocatalyst under N_2- and CO_2-saturated solutions. (b) DRS spectra of Co_9S_8, $Ru(bpy)_3^{2+}$ and $Ru(bpy)_3^{2+}/Co_9S_8$ hybrid. (c) Mott–Schottky plots. (d) Schematic illustration of energy levels and electron transfer from the ruthenium photosensitizer to the Co_9S_8 cocatalyst. (e) PL spectra and (f) transient photocurrent generation of reaction systems with and without the Co_9S_8 cocatalyst.

band potential of Co_9S_8 was estimated by electrochemical Mott–Schottky plots. As shown in Fig. 7c, the derived CBM potential of the Co_9S_8 cocatalyst is about −0.71 V (*vs.* NHE, pH = 7.0), which integrated with the bandgap energy determines its VBM position at about 0.27 V (*vs.* NHE, pH = 7.0). Regarding the band structure of Co_9S_8, the lowest unoccupied molecular orbital (LUMO) and highest occupied molecular orbital (HOMO) levels of $Ru(bpy)_3^{2+}$, and the redox potential for reducing CO_2 to CO (Fig. 7d),[26,62,66] the excited electrons of the photosensitizer are encouraged thermo-dynamically to travel to the cocatalyst for driving the CO_2 reduction reaction.

To monitor the separation and transport of light-excited charges in the photochemical system, room temperature photoluminescence (PL) was implemented. As revealed in Fig. 7e, the system involving Co_9S_8 reveals a quenched PL emission compared to the system free of the cocatalyst, suggesting the prohibited recombination of light-stimulated charges of the former.[31,40] Simultaneously, the time-resolved PL (TRPL) spectra (Fig. S5, ESI†) reveal that the average emission lifetime of the reaction mixture with the cocatalyst (399 ns) is much shorter than that of the mixture without its presence (450 ns), indicating that quick electron transfer exists between the photosensitizer and the cocatalyst. Consistently, the photocurrent generation of the Co_9S_8-mediated system is higher than that of the system without its existence (Fig. 7f), which mirrors the boosted transport of charge carriers induced by the metal

sulfide cocatalyst.[26,47,67] All the above results show that the Co_9S_8 cocatalyst can expedite separation and transfer of light-excited charges and promote activation of CO_2 molecules, thus reinforcing the CO_2 photoreduction efficiency.

Density functional theory (DFT) calculations were carried out to gain some insights into the interaction between the $Ru(bpy)_3^{2+}$ photosensitizer and Co_9S_8 cocatalyst. The results prove that the $Ru(bpy)_3^{2+}$ complex can be strongly adsorbed on the Co_9S_8 (311) surface, in which the carbon atoms of $Ru(bpy)_3^{2+}$ and the surface Co atoms of Co_9S_8 form four Co–C bonds with a length of about 2.1 Å (Fig. 8). The chemical bonds between the photosensitizer and the cocatalyst may serve as the "bridges" to guarantee quick electron migration from the excited photosensitiser to the active Co_9S_8 cocatalyst to run the CO_2 reduction reaction.

Finally, we have proposed a probable mechanism of the CO_2 photoreduction reaction catalyzed by the caged Co_9S_8 cocatalyst. Being stimulated by visible light illumination, the ground state photosensitizer $Ru(bpy)_3^{2+}$ moves to the excited state of $Ru(bpy)_3^{2+}*$. Such an excited state will react with the electron donor TEOA through a reductive quenching process, leading to the formation of the photosensitizer in a reduced state of $Ru(bpy)_3^+$.[26,64] The excited electrons of the $Ru(bpy)_3^+$ species will delocalize and move to the porous Co_9S_8 cocatalyst to run the CO_2-to-CO conversion reaction,[60,62,65] during which the Co_9S_8 cages not only strengthen the adsorption and activation of CO_2 molecules but also push the separation and migration of light-generated charges to support the reaction.

In summary, well-defined dodecahedral Co_9S_8 cages have been fabricated and applied as a new cocatalyst for CO_2 photoreduction with visible light. Owing to the high surface area and plentiful catalytically reactive locations, the hollow C_9S_8 cocatalyst effectively boosts CO_2 activation and prevents charge recombination. In a classic light-sensitized system, such a non-noble-metal cocatalyst can powerfully promote the conver-
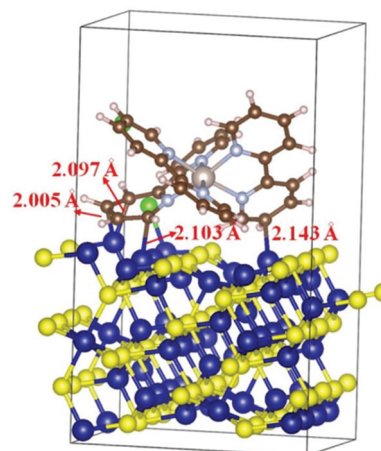

Fig. 8 The structure of $Ru(bpy)_3Cl_2$ adsorbed on the Co_9S_8 (311) surface with an adsorption energy of −4.5 eV. The Co, S, Ru, N, C, H, and Cl atoms are denoted by blue, yellow, pink, gray, brown, white, and green, respectively.

sion of CO_2 to CO with high efficiency and good stability. Inspired by this contribution, future studies about the sulfide semiconductors with narrow bandgaps and the hybrids of Co_9S_8/semiconductor for photocatalytic CO_2 reduction may be anticipated.

Author contributions

Xiahui Lin: conceptualization, methodology, feasibility analysis, validation, writing-original draft, and writing-review and editing. Zidong Xie: methodology, feasibility analysis, and validation. Bo Su: methodology, validation, and writing-review and editing. Mei Zheng: theoretical calculation. Wenxin Dai: feasibility analysis. Yidong Hou: writing-review and editing. Zhengxin Ding: writing-review and editing. Wei Lin: theoretical calculation and supervision. Yuanxing Fang: writing-review and editing and supervision. Sibo Wang: validation, writing-review and editing, and supervision.

Conflicts of interest

There are no conflicts of interest to declare.

Acknowledgements

Notes and references

1 J. L. White, M. F. Baruch, J. E. Pander, Y. Hu, I. C. Fortmeyer, J. E. Park, T. Zhang, K. Liao, J. Gu, Y. Yan, T. W. Shaw, E. Abelev and A. B. Bocarsly, *Chem. Rev.*, 2015, **115**, 12888–12935.
2 K. Niu, Y. Xu, H. Wang, R. Ye, H. L. Xin, F. Lin, C. Tian, Y. Lum, K. C. Bustillo, M. M. Doeff, M. T. M. Koper, J. Ager, R. Xu and H. Zheng, *Sci. Adv.*, 2017, **3**, e1700921.
3 S. C. Shit, I. Shown, R. Paul, K.-H. Chen, J. Mondal and L.-C. Chen, *Nanoscale*, 2020, **12**, 23301–23332.
4 L. Huang, B. Li, B. Su, Z. Xiong, C. Zhang, Y. Hou, Z. Ding and S. Wang, *J. Mater. Chem. A*, 2020, **8**, 7177–7183.
5 Y. Fang, Y. Zheng, T. Fang, Y. Chen, Y. Zhu, Q. Liang, H. Sheng, Z. Li, C. Chen and X. Wang, *Sci. China: Chem.*, 2020, **63**, 149–181.
6 W. Zhang, A. R. Mohamed and W.-J. Ong, *Angew. Chem.*, 2020, **59**, 22894–22915.
7 W. Zhang, R. Huang, L. Song and X. Shi, *Nanoscale*, 2021, **13**, 9075–9090.
8 M. Ou, W. Tu, S. Yin, W. Xing, S. Wu, H. Wang, S. Wan, Q. Zhong and R. Xu, *Angew. Chem., Int. Ed.*, 2018, **57**, 13570–13574.
9 Y. Fang and X. Wang, *Chem. Commun.*, 2018, **54**, 5674–5687.
10 G. Lin, L. Sun, G. Huang, Q. Chen, S. Fang, J. Bi and L. Wu, *Sustainable Energy Fuels*, 2021, **5**, 732–739.
11 K. Maeda, *Adv. Mater.*, 2019, **31**, 1808205.
12 G. Zhang, Z. Wang and J. Wu, *Nanoscale*, 2021, **13**, 4359–4389.
13 B. Luo, G. Liu and L. Wang, *Nanoscale*, 2016, **8**, 6904–6920.
14 W.-J. Ong, L. K. Putri and A. R. Mohamed, *Chem. – Eur. J.*, 2020, **26**, 9710–9748.
15 A. Nakada, H. Kumagai, M. Robert, O. Ishitani and K. Maeda, *Acc. Mater. Res.*, 2021, **2**, 458–470.
16 Y. Ma, Y. Fang, X. Fu and X. Wang, *Sustainable Energy Fuels*, 2020, **4**, 5812–5817.
17 J. Ran, M. Jaroniec and S.-Z. Qiao, *Adv. Mater.*, 2018, **30**, 1704649.
18 S. Wang, J. Lin and X. Wang, *Phys. Chem. Chem. Phys.*, 2014, **16**, 14656–14660.
19 L. Wei, J. Lin, S. Xie, W. Ma, Q. Zhang, Z. Shen and Y. Wang, *Nanoscale*, 2019, **11**, 12530–12536.
20 Q. Zhai, S. Xie, W. Fan, Q. Zhang, Y. Wang, W. Deng and Y. Wang, *Angew. Chem., Int. Ed.*, 2013, **52**, 5776–5779.
21 C. Tsounis, R. Kuriki, K. Shibata, J. J. M. Vequizo, D. Lu, A. Yamakata, O. Ishitani, R. Amal and K. Maeda, *ACS Sustainable Chem. Eng.*, 2018, **6**, 15333–15340.
22 Y.-X. Chen, Y.-F. Xu, X.-D. Wang, H.-Y. Chen and D.-B. Kuang, *Sustainable Energy Fuels*, 2020, **4**, 2249–2255.
23 K. Zhao, S. Zhao, C. Gao, J. Qi, H. Yin, D. Wei, M. F. Mideksa, X. Wang, Y. Gao, Z. Tang and R. Yu, *Small*, 2018, **14**, 1800762.
24 Q. Li, F. Lin, F. Liu and X. Wang, *Chem. Commun.*, 2019, **55**, 3903–3906.
25 B. Han, X. Ou, Z. Deng, Y. Song, C. Tian, H. Deng, Y.-J. Xu and Z. Lin, *Angew. Chem., Int. Ed.*, 2018, **57**, 16811–16815.
26 X. Lin, S. Wang, W. Tu, H. Wang, Y. Hou, W. Dai and R. Xu, *ACS Appl. Energy Mater.*, 2019, **2**, 7670–7678.
27 D. Hong, T. Kawanishi, Y. Tsukakoshi, H. Kotani, T. Ishizuka and T. Kojima, *J. Am. Chem. Soc.*, 2019, **141**, 20309–20317.
28 J. Di, C. Chen, C. Zhu, P. Song, M. Duan, J. Xiong, R. Long, M. Xu, L. Kang, S. Guo, S. Chen, H. Chen, Z. Chi, Y.-X. Weng, H. Li, L. Song, M. Wu, Q. Yan, S. Li and Z. Liu, *Nano Energy*, 2021, **79**, 105429.
29 R. Xu, H. Xu, S. Ning, Q. Zhang, Z. Yang and J. Ye, *Trans. Tianjin Univ.*, 2020, **26**, 470–478.
30 C. Qiu, S. Bai, W. Cao, L. Tan, J. Liu, Y. Zhao and Y.-F. Song, *Trans. Tianjin Univ.*, 2020, **26**, 352–361.
31 B. Su, L. Huang, Z. Xiong, Y. Yang, Y. Hou, Z. Ding and S. Wang, *J. Mater. Chem. A*, 2019, **7**, 26877–26883.
32 S. Wang, Y. Wang, S. L. Zhang, S. Q. Zang and X. W. Lou, *Adv. Mater.*, 2019, **31**, 1903404.
33 M. Xiao, Z. Wang, M. Lyu, B. Luo, S. Wang, G. Liu, H.-M. Cheng and L. Wang, *Adv. Mater.*, 2019, **31**, 1801369.
34 Y. Wang, S. Wang, S. L. Zhang and X. W. Lou, *Angew. Chem.*, 2020, **59**, 11918–11922.
35 Y. Wang, S. Wang and X. W. Lou, *Angew. Chem., Int. Ed.*, 2019, **58**, 17236–17240.

36 S. Wang, B. Y. Guan, Y. Lu and X. W. Lou, *J. Am. Chem. Soc.*, 2017, **139**, 17305–17308.

37 S. Wang, Y. Wang, S.-Q. Zang and X. W. Lou, *Small Methods*, 2020, **4**, 1900586.

38 C. Bie, B. Zhu, F. Xu, L. Zhang and J. Yu, *Adv. Mater.*, 2019, **31**, 1902868.

39 L. Wang, J. Wan, Y. Zhao, N. Yang and D. Wang, *J. Am. Chem. Soc.*, 2019, **141**, 2238–2241.

40 S. Wang, B. Y. Guan and X. W. Lou, *J. Am. Chem. Soc.*, 2018, **140**, 5037–5040.

41 P. Zhang, S. Wang, B. Y. Guan and X. W. Lou, *Energy Environ. Sci.*, 2019, **12**, 164–168.

42 Z. Wang, S. A. Monny and L. Wang, *ChemNanoMat*, 2020, **6**, 881–888.

43 X. Liu, M. Ye, S. Zhang, G. Huang, C. Li, J. Yu, P. K. Wong and S. Liu, *J. Mater. Chem. A*, 2018, **6**, 24245–24255.

44 H. Hu, L. Han, M. Yu, Z. Wang and X. W. Lou, *Energy Environ. Sci.*, 2016, **9**, 107–111.

45 H. Hu, B. Guan, B. Xia and X. W. Lou, *J. Am. Chem. Soc.*, 2015, **137**, 5590–5595.

46 S. Wang, B. Y. Guan, X. Wang and X. W. Lou, *J. Am. Chem. Soc.*, 2018, **140**, 15145–15148.

47 B. Qiu, Q. Zhu, M. Du, L. Fan, M. Xing and J. Zhang, *Angew. Chem., Int. Ed.*, 2017, **56**, 2684–2688.

48 G. Zhang, D. Chen, N. Li, Q. Xu, H. Li, J. He and J. Lu, *Angew. Chem.*, 2020, **59**, 8255–8261.

49 T. P. Yendrapati, J. Soumya, S. Bojja and U. Pal, *J. Phys. Chem. C*, 2021, **125**, 5099–5109.

50 P. Tan, Y. Liu, A. Zhu, W. Zeng, H. Cui and J. Pan, *ACS Sustainable Chem. Eng.*, 2018, **6**, 10385–10394.

51 L. Shen, L. Yu, H. B. Wu, X.-Y. Yu, X. Zhang and X. W. Lou, *Nat. Commun.*, 2015, **6**, 6694.

52 L.-L. Feng, G.-D. Li, Y. Liu, Y. Wu, H. Chen, Y. Wang, Y.-C. Zou, D. Wang and X. Zou, *ACS Appl. Mater. Interfaces*, 2015, **7**, 980–988.

53 S. Zhang, D. Zhai, T. Sun, A. Han, Y. Zhai, W.-C. Cheong, Y. Liu, C. Su, D. Wang and Y. Li, *Appl. Catal., B*, 2019, **254**, 186–193.

54 S. Wang, B. Y. Guan and X. W. Lou, *Energy Environ. Sci.*, 2018, **11**, 306–310.

55 S. Wang, Y. Hou and X. Wang, *ACS Appl. Mater. Interfaces*, 2015, **7**, 4327–4335.

56 W. Wei, W. Chen and D. G. Ivey, *Chem. Mater.*, 2008, **20**, 1941–1947.

57 S. Wang, W. Yao, J. Lin, Z. Ding and X. Wang, *Angew. Chem., Int. Ed.*, 2014, **53**, 1034–1038.

58 W. Yang, H.-J. Wang, R.-R. Liu, J.-W. Wang, C. Zhang, C. Li, D.-C. Zhong and T.-B. Lu, *Angew. Chem.*, 2021, **60**, 409–414.

59 T. Ouyang, H.-J. Wang, H.-H. Huang, J.-W. Wang, S. Guo, W.-J. Liu, D.-C. Zhong and T.-B. Lu, *Angew. Chem., Int. Ed.*, 2018, **57**, 16480–16485.

60 J. Nai, S. Wang and X. W. Lou, *Sci. Adv.*, 2019, **5**, eaax5095.

61 Q. Mu, W. Zhu, G. Yan, Y. Lian, Y. Yao, Q. Li, Y. Tian, P. Zhang, Z. Deng and Y. Peng, *J. Mater. Chem. A*, 2018, **6**, 21110–21119.

62 P. Niu, Z. Pan, S. Wang and X. Wang, *ChemSusChem*, 2021, **14**, 1302–1307.

63 S. Wang, Z. Ding and X. Wang, *Chem. Commun.*, 2015, **51**, 1517–1519.

64 Y. Su, Z. Song, W. Zhu, Q. Mu, X. Yuan, Y. Lian, H. Cheng, Z. Deng, M. Chen, W. Yin and Y. Peng, *ACS Catal.*, 2021, **11**, 345–354.

65 P. Niu, Z. Pan, S. Wang and X. Wang, *ChemCatChem*, 2021, **13**, 3581–3587.

66 X. Lin, Y. Gao, M. Jiang, Y. Zhang, Y. Hou, W. Dai, S. Wang and Z. Ding, *Appl. Catal., B*, 2018, **224**, 1009–1016.

67 B. Li, W. Wang, J. Zhao, Z. Wang, B. Su, Y. Hou, Z. Ding, W.-J. Ong and S. Wang, *J. Mater. Chem. A*, 2021, **9**, 10270–10276.